NANO LETTERS

pubs.acs.org/NanoLett Letter

Self-Cascade Uricase/Catalase Mimics Alleviate Acute Gout

Anqi Lin,[‖] Ziying Sun,[‖] Xingquan Xu, Sheng Zhao, Jiawei Li, Heng Sun, Quan Wang, Qing Jiang, Hui Wei,* and Dongquan Shi*

Cite This: *Nano Lett.* 2022, 22, 508−516 Read Online

ACCESS | Metrics & More | Article Recommendations | Supporting Information

ABSTRACT: Uricase-based therapies are limited for gout partially due to the accumulation of H_2O_2 in an arthrosis environment with slow metabolism. To tackle this limitation, previous studies adopted a cascade reaction between the degradation of uric acid (UA) and timely elimination of H_2O_2 using complicated composites of uricase and catalase (CAT)/CAT-like nanozyme. Herein, the self-cascade nanozyme Pt/CeO_2 with high efficiency toward simultaneous UA degradation and H_2O_2 elimination is demonstrated on the basis of both uricase- and CAT-like activities in Pt, Ir, Rh, and Pd platinum-group metals. With an optimized molar ratio of Pt and CeO_2, Pt/CeO_2 (1/5) not only does better in degrading UA but also has excellent reactive oxygen species (ROS) and reactive nitrogen species (RNS) scavenging activities. In monosodium urate (MSU)-induced acute gout rats, Pt/CeO_2 nanozyme markedly alleviates pain along with joint edema, thus improving gait claudication and tissue inflammation. These results provide novel insights into strategies of an efficient enzyme-mimetic treatment for gout.

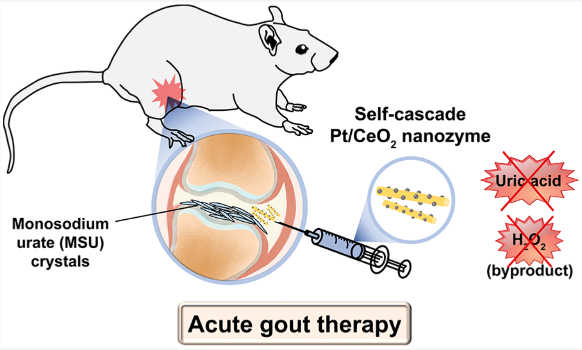

KEYWORDS: *Self-cascade nanozyme, Platinum-group metal, Uric acid degradation, H_2O_2 elimination, Acute gout*

1. INTRODUCTION

Gout is a common inflammatory arthritis due to purine metabolism and lifestyle factors.[1−3] The deposition of monosodium urate (MSU) crystals, a crystallized form of uric acid (UA), in peripheral joints and periarticular tissues causes intense pain and drastic inflammatory response.[2,4−6] However, the concentration of UA in tissues always keeps increasing until saturation due to the uricase deficiency in humans. The current treatment for gout includes the temporary relief of pain and inflammation of an acute attack (nonsteroidal anti-inflammatory drugs, colchicine, and corticosteroids) and a long-term UA-lowering therapy (uricase agent and nonenzyme drugs).[7] Surgical intervention is considered if the joint symptoms are out of control because of severe MSU deposition.

Uricase catalyzes the degradation of UA to allantoin, which is more water-soluble. Therefore, a uricase-based therapy has been explored as an effective and emerging strategy to treat gout. As an exogenous enzyme, uricase is immunogenic to humans. To minimize the immunogenic effect, various strategies such as uricase surface modification were developed.[8−11] Encouragingly, pegloticase (a PEGlyated uricase) has achieved the Food and Drug Administration approval for treating chronic refractory gout in 2010.[12] Nevertheless, the PEGylated uricase still has some drawbacks (*e.g.*, 89% antibody occurrence and adverse cardiovascular events).[13] Moreover, uricase-mediating uricolysis generates hydrogen peroxide (H_2O_2) as a byproduct. Particularly, slow metabolism in the articular cavity and the closed internal environment markedly aggravate the accumulation of H_2O_2. This leads to not only oxidative stress in cells but also chronic joint damage. Thus, the timely elimination of H_2O_2 during UA degradation is essential for uricase-based therapies. Recently, a few studies focus on the cascade reaction system of uricase and catalase (CAT) (or CAT-like nanozyme) to maximize the therapeutic efficacy by eliminating UA and H_2O_2 sequentially.[14−17] Nevertheless, those systems adopt a spatially confined structure to fulfill the biocompatibility *in vivo* and to maintain the activities of two encapsulated substances, which requires a delicate and complicated design. Hence, selecting a multifunctional nanozyme with UA degradation as well as H_2O_2 scavenging activities could achieve a self-cascade reaction in joints, providing an effective strategy for the treatment of gout.

Nanozymes have attracted increasing attention in biomedical applications due to multienzyme-like activities, high stability, and low cost.[18−21] For example, Fe-N_4-C artificial peroxisome was used to ameliorate UA-related hyperuricemia and ischemic stroke.[21] Recent *in vitro* studies revealed that

Received: November 18, 2021
Revised: December 18, 2021
Published: December 30, 2021

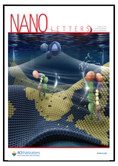

https://doi.org/10.1021/acs.nanolett.1c04454

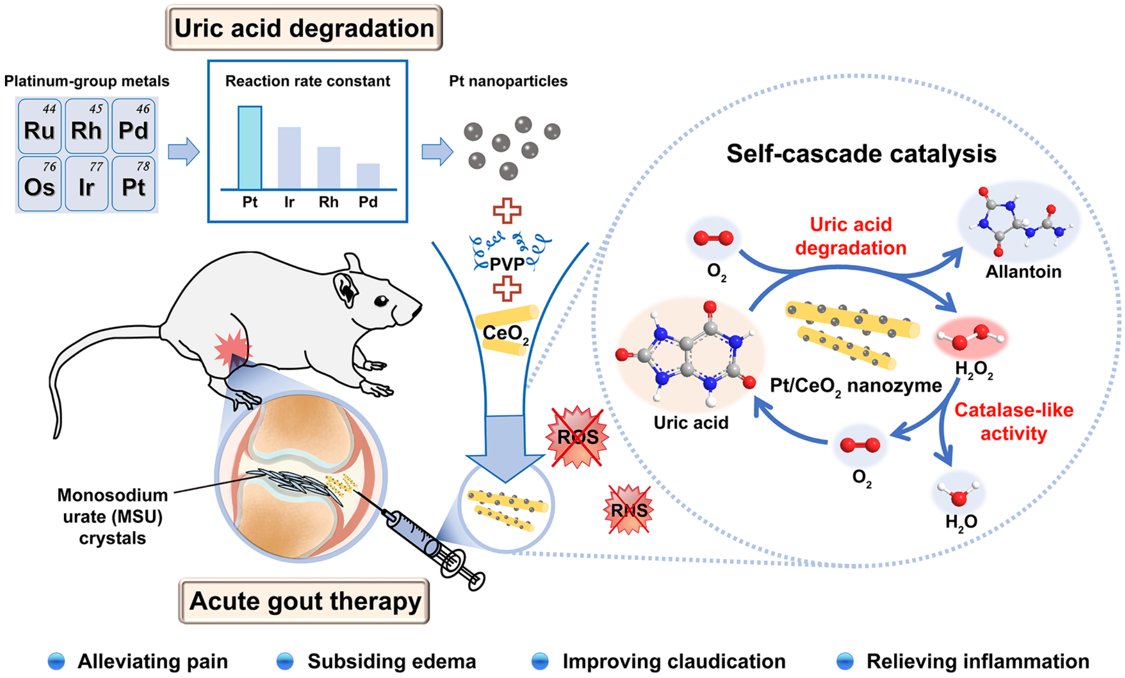

Figure 1. Schematic illustration of the design and synthesis of the Pt/CeO$_2$ nanozyme based on platinum-group metals and self-cascade uric acid degradation for MSU-induced acute gout therapy.

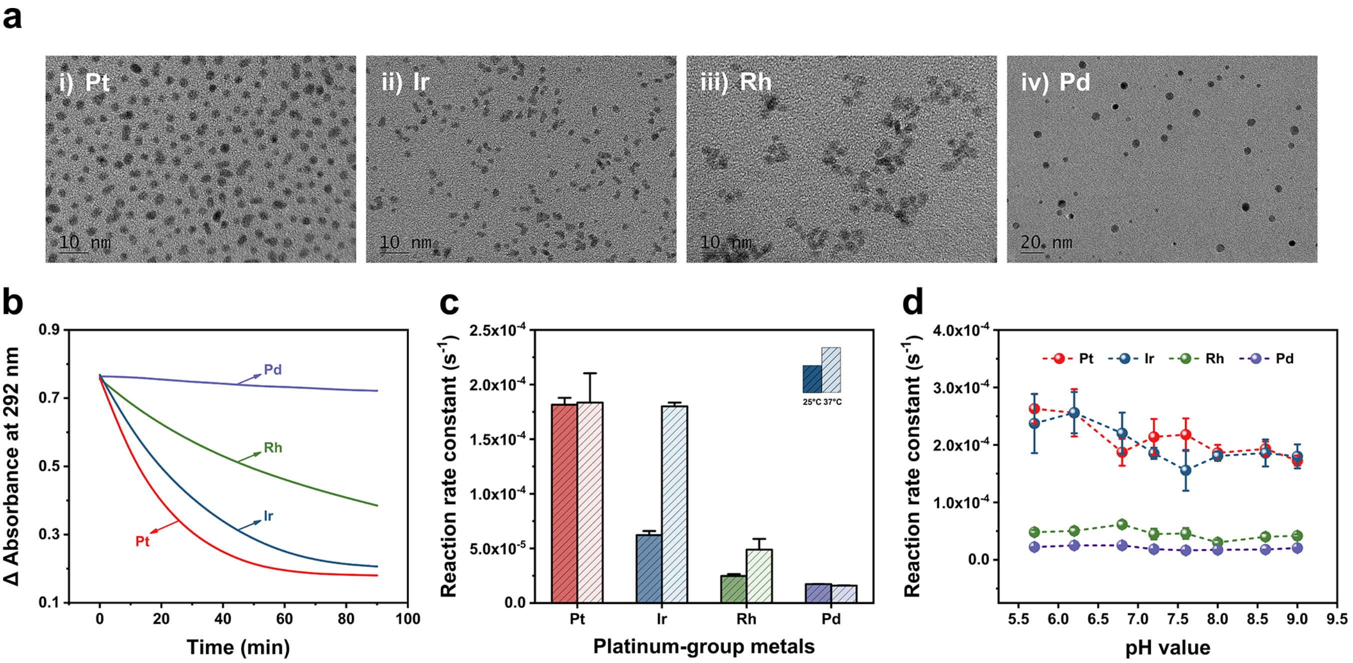

Figure 2. Characterization and UA degradation activities of platinum-group metals. (a) TEM images of Pt, Ir, Rh, and Pd NPs. (b) Changes in absorbance at 292 nm every 10 min recorded by UV−vis spectra for the catalytic degradation of UA by the four metals. Results are expressed as Δ(absorbance) = (absorbance measured during UA degradation) − (background absorbance of metals). (c) UA degradation activities of the four metals at 25 and 37 °C. (d) UA degradation activities of the four metals at different pH values. In (b−d), the amounts of materials used were normalized by the corresponding metal content. A 20 μg/mL amount of the four metals was used for (b−d). A 50 μM amount of UA was used for (b), and 100 μM of UA was used for (c) and (d). Tests of (b) and (d) were carried out at 37 °C.

nanosized Pt is an active uricase mimic.[22,23] It is reasonable to investigate the uricase-like activity of subordinative platinum-group metals (*e.g.*, Ir, Rh, and Pd). Yet, few studies have developed a nanozyme as a therapeutic agent for alleviating gout. On the other hand, Pt and other platinum-group metals are promising CAT mimics to eliminate H_2O_2.[24−27] We reason that one could screen the most suitable metal on the basis of the self-cascade catalysis of uricolysis to alleviate gout.

Herein, to simultaneously address acute pain and MSU deposition, two major issues in the treatment of gout, we demonstrate that Pt shows excellent capability for UA degradation under physiological conditions, in comparison with Ir, Rh, and Pd. To offer more stability and

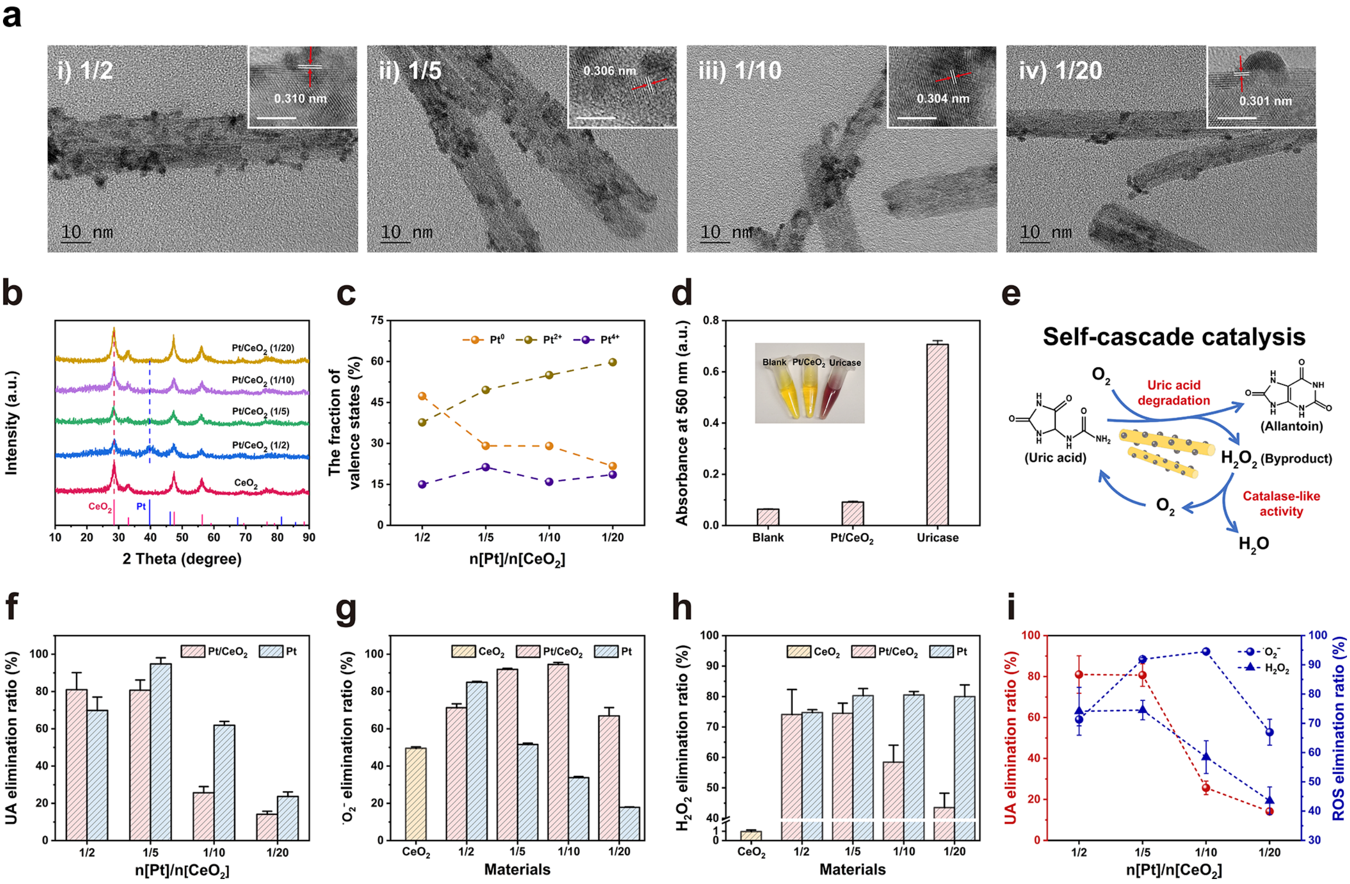

Figure 3. Characterization and diverse catalytic activities of Pt/CeO$_2$ with different molar ratios. (a) TEM images. The insets are HR-TEM images of Pt/CeO$_2$ with the corresponding ratios. Scale bar: 5 nm. (b) Powder XRD patterns. The pink and blue lines at the bottom mark the reference patterns of CeO$_2$ and Pt from the JCPDS database, Card Nos. 43-1002 and 04−0802, respectively. (c) Changes in the fraction of Pt valence states in Pt/CeO$_2$. (d) Detection of accumulated H$_2$O$_2$ after catalysis of the reaction by Pt/CeO$_2$ and uricase. A 100 μM amount of UA, Pt content at 20 μg/mL of Pt/CeO$_2$ (1/5) and 1 U/mL of uricase were used for UA degradation at 37 °C for 90 min. The inset is a digital photograph of the FOX assay on different samples. The color of solution changes from yellow to purple in the presence of H$_2$O$_2$. (e) Schematic illustration of the self-cascade catalysis by Pt/CeO$_2$. (f) Percentage of UA elimination catalyzed by the indicated materials. (g) Percentage of superoxide radical elimination catalyzed by the SOD-like activity of the indicated materials. (h) Percentage of H$_2$O$_2$ elimination catalyzed by the CAT-like activity of the indicated materials. (i) Comparison of several activities of Pt/CeO$_2$ with different molar ratios. The amounts of materials used in (f) and (g) were normalized by CeO$_2$ content (80 μg/mL). Pt alone was used as an equal amount of Pt in Pt/CeO$_2$ with the corresponding ratio. Pt contents in Pt/CeO$_2$ with different molar ratios were 50.8 μg/mL (1/2), 19.4 μg/mL (1/5), 9.76 μg/mL (1/10) and 4.80 μg/mL (1/20), respectively. Amounts of materials used in (h) were half of those used in (f) and (g).

biocompatibility for *in vivo* applications, CeO$_2$ nanorods were chosen as the supporting substrates and polyvinylpyrrolidone (PVP) with random-coiled chains as a "guiding molecule" to evenly grow Pt *in situ* on CeO$_2$ nanorods. By optimizing the molar ratio of Pt and CeO$_2$, we show that Pt/CeO$_2$ (1/5) not only does better in degrading UA on the basis of a self-cascade catalysis but also has excellent reactive oxygen species (ROS) and reactive nitrogen species (RNS) scavenging activities. In MSU-induced acute gout rats, Pt/CeO$_2$ nanozyme alleviates pain along with joint edema, thus improving gait claudication and tissue inflammation (Figure 1).

2. RESULTS AND DISCUSSION

2.1. Synthesis, Characterization, and UA Degradation of Pt, Ir, Rh, and Pd. The formations of Pt, Ir, Rh, and Pd nanoparticles (NPs) were first confirmed by transmission electron microscopy (TEM) imaging and powder X-ray diffraction (XRD) (Figure 2a and Figures S1 and S2). The Pt, Ir, Rh, and Pd NPs were approximately spherical with average sizes of 2.9, 1.9, 3.8, and 5.2 nm, respectively (Figure S1b−e). High-resolution TEM images indicated the adjacent fringes of 0.220, 0.213, 0.222, and 0.215 nm that were assigned to the lattice spacing of the (111) facets of the face-centered-cubic (fcc) Pt, Ir, Rh, and Pd NPs, respectively (Figure S1a). Dynamic lighting scattering (DLS) (Figure S3) and ζ potential (Figure S4) results of the four newly prepared metals demonstrated their good monodispersity in water due to the stabilization of PVP.

Afterward, the NP-catalyzed degradation of UA was evaluated by monitoring the decrease in absorbance at 292 nm, the characteristic absorbance of UA. As we hypothesized above, Ir, Rh, and Pd NPs could also catalyze the oxidative degradation of UA similarly to Pt NPs, while Pt NPs catalysis was the fastest in comparison with other NPs with a trend of Pt > Ir > Rh > Pd (Figure 2b and Figure S5). The UA degradation activity of the NPs was further evaluated by a subsequent kinetics analysis. The degradation is governed by a first-order reaction (eq 1)[22]

$$k = \frac{1}{t}\ln\frac{c_0}{c_t} \qquad (1)$$

where k is the reaction rate constant, t is the degradation time, c_0 is the initial concentration of UA, and c_t is the residual concentration of UA. The reaction rate constant k was calculated in the first 40 min. We found that Pt NPs presented the highest activity of degrading UA at around room temperature (25−30 °C), while Pt NPs as well as Ir NPs had similarly better performance around and above physiological temperature (35−45 °C) (Figure 2c and Figure S6). However, both Rh NPs and Pd NPs maintained lower catalytic activities with slight fluctuations in the range of 25−45 °C. When they were in different pH environments (Figure 2d), both Pt NPs and Ir NPs showed higher performance in acidic pH in comparison to those in more basic pH. Moreover, Pt NPs did better in weakly alkaline systems, which is closer to the physiological environment. There is almost no fluctuation in the catalytic activities of Rh NPs and Pd NPs at different pH values. Since Pt possessed excellent capability for UA degradation, we chose Pt as a therapeutic component to rationally design a nanozyme to alleviate gout.

2.2. Synthesis and Characterization of Pt/CeO$_2$. Metal NPs fixed on specific substrates should facilitate their stability in complex environments. In addition, highly tunable properties containing metal−substrate interactions and a certain number of defects may activate additional catalytic sites different from the case for the metal or substrate alone.[28−31] Herein, CeO$_2$ was selected as a favorable supporting substrate for biomedical applications due to its extraordinary biocompatibility, adjustable morphology, and ROS scavenging abilities.[32−36] For convenient fabrication on a large scale, we chose CeO$_2$ nanorods as the supporting substrates presynthesized by a hydrothermal method.[34] Particularly, CeO$_2$ nanorods expose more (111) facets in the axial lateral area, facilitating *in situ* nucleation of Pt. In addition, PVP was selected as a “guiding molecule” to evenly decentralize the nucleation and growth of Pt on nanorods.

The amount of PVP used is crucial for the controlled morphology of Pt/CeO$_2$. We first fixed the n[Pt]/n[CeO$_2$] molar ratio at 1/10, and then different samples were synthesized with n[Pt]/n[PVP] molar ratios of 1/30, 1/60, and 1/90 and without PVP. There was an obvious change in morphology with different amounts of PVP, as shown in TEM images (Figure S7). We observed that Pt tended to form larger clusters (about 10−40 nm) on CeO$_2$ nanorods without PVP (Figure S7a). As the amount of PVP increased, the nucleation of Pt was decentralized by the disturbance of PVP with random-coiled chains; thus, *in situ* growth transformed into smaller NPs (about 3−5 nm) (Figure S7b,c). However, there were fewer Pt NPs formed on CeO$_2$ nanorods due to severe interference when excess PVP was added during nucleation of Pt (Figure S7d). In addition, the addition of PVP decreased the ζ potential of Pt/CeO$_2$, whereas a further increased amount of PVP had almost no influence on the ζ potential (Figure S8a). We speculated that PVP mainly worked in the initial nucleation of Pt and only a small part grafted on Pt/CeO$_2$ to stabilize the growth of Pt. On the basis of the results above, a n[Pt]/n[PVP] molar ratio of 1/60 was selected to synthesize Pt *in situ* that had sizes similar to those of the Pt NPs above.

Then, Pt/CeO$_2$ with different molar ratios of Pt and CeO$_2$ was synthesized (n[Pt]/n[CeO$_2$] = 1/2, 1/5, 1/10, 1/20) and characterized by TEM images, powder XRD, ζ potential, and X-ray photoelectron spectra (XPS) (Figure 3a−c and Figures S8b and S9−S12). CeO$_2$ nanorods and Pt alone without modifications were used as control groups (TEM images are shown in Figure S13). As shown in Figure 3a, lattice fringes of 0.310, 0.306, 0.304, and 0.301 nm were all assigned to the spacing of CeO$_2$ (111) facets (JCPDS No. 43-1002). We inferred that preferred nucleation sites could be provided at the (111) facets of CeO$_2$ nanorods, thus facilitating the *in situ* growth of Pt.[28,29] With an increasing content of Pt in Pt/CeO$_2$, the distribution of Pt on nanorods tended to be denser and the ζ potential of Pt/CeO$_2$ gradually decreased from 15.8 mV (1/20) to −2.5 mV (1/2) (Figure S8b).

In more detail, the composition and variation of charge states of the elements were analyzed by XPS analysis. The survey spectrum confirmed the presence of Ce, Pt, and O elements in CeO$_2$ or Pt/CeO$_2$ (Figure S9). As shown in Figure S10, there was only a slight fluctuation in the fraction of Ce^{3+} between CeO$_2$ and Pt/CeO$_2$. However, it was observed that the oxidative states of Pt^{2+} were present at a high percentage and the state of Pt^{4+} also appeared with a small amount in the Pt 4f fitted spectra of Pt/CeO$_2$ (Figure S11). Moreover, the increasing content of Pt in Pt/CeO$_2$ triggered a significant decrease in the fraction of Pt^{2+} while there was an obvious increase in the fraction of Pt^0 (Figure 3c). Hence, it appeared that the deposition of PtO$_x$ particles tended to occur during *in situ* growth of Pt on CeO$_2$ nanorods.

Due to the formation of the PtO$_x$/CeO$_2$ system, new oxygen components appeared in the fitted O 1s spectra of Pt/CeO$_2$ (Figure S12 and annotated in Table S1). In the fitted O 1s spectrum of CeO$_2$, the curves were deconvoluted into three peaks, which were attributed to the lattice oxygen (O$_\alpha$), surface oxygen species related to defects (O$_\beta$), and the absorbed oxygen (O$_\gamma$) (Figure S12a).[37,38] However, in the fitted curves of Pt/CeO$_2$, the O 1s spectra consisted of four peaks (Figure S12b−e). The state O$_{\mathrm{I}}$ was attributed to the lattice oxygen, similar to O$_\alpha$ in CeO$_2$. The new form O$_{\mathrm{II}}$ was more likely due to oxygen binding either to Pt or simultaneously to Pt and CeO$_2$ at the surface.[39,40] The peak O$_{\mathrm{III}}$ most probably referred to surface oxygen species related to defects and the amount of carbonyl groups in PVP.[40,41] The O$_{\mathrm{IV}}$ form was likely due to the chemisorbed water and/or hydroxyl groups in PVP.[41,42] These results indicated that the new forms of defects introduced by Pt might work toward diverse enzyme-like activities of Pt/CeO$_2$, including the adsorption of different substrate molecules around them.

2.3. Self-Cascade UA Degradation, ROS Scavenging, and RNS Eliminating Activities of Pt/CeO$_2$. Considering UA degradation and CAT-like activities of Pt in Pt/CeO$_2$ simultaneously,[22,24] we first verified the self-cascade reaction during the degrading process of UA via ferrous oxidation in a xylenol orange (FOX) assay (Figure 3d). A catalytic reaction involving uricase inevitably caused the accumulation of H$_2$O$_2$, leading to a color change of the FOX reagent from yellow to deep red. However, due to the CAT-like activity of Pt, the byproduct H$_2$O$_2$ could be consumed in a timely fashion and a self-cascade reaction formed through this step. Thus, there was almost no residual H$_2$O$_2$ detected by the FOX reagent. Further, allantoin could be observed as the reaction product from the catalysis of Pt using ultra-performance liquid chromatography−mass spectrometry (UPLC-MS). It is worth noting that allantoin was the same as the degradation product from natural uricase, and the schematic illustration of the self-

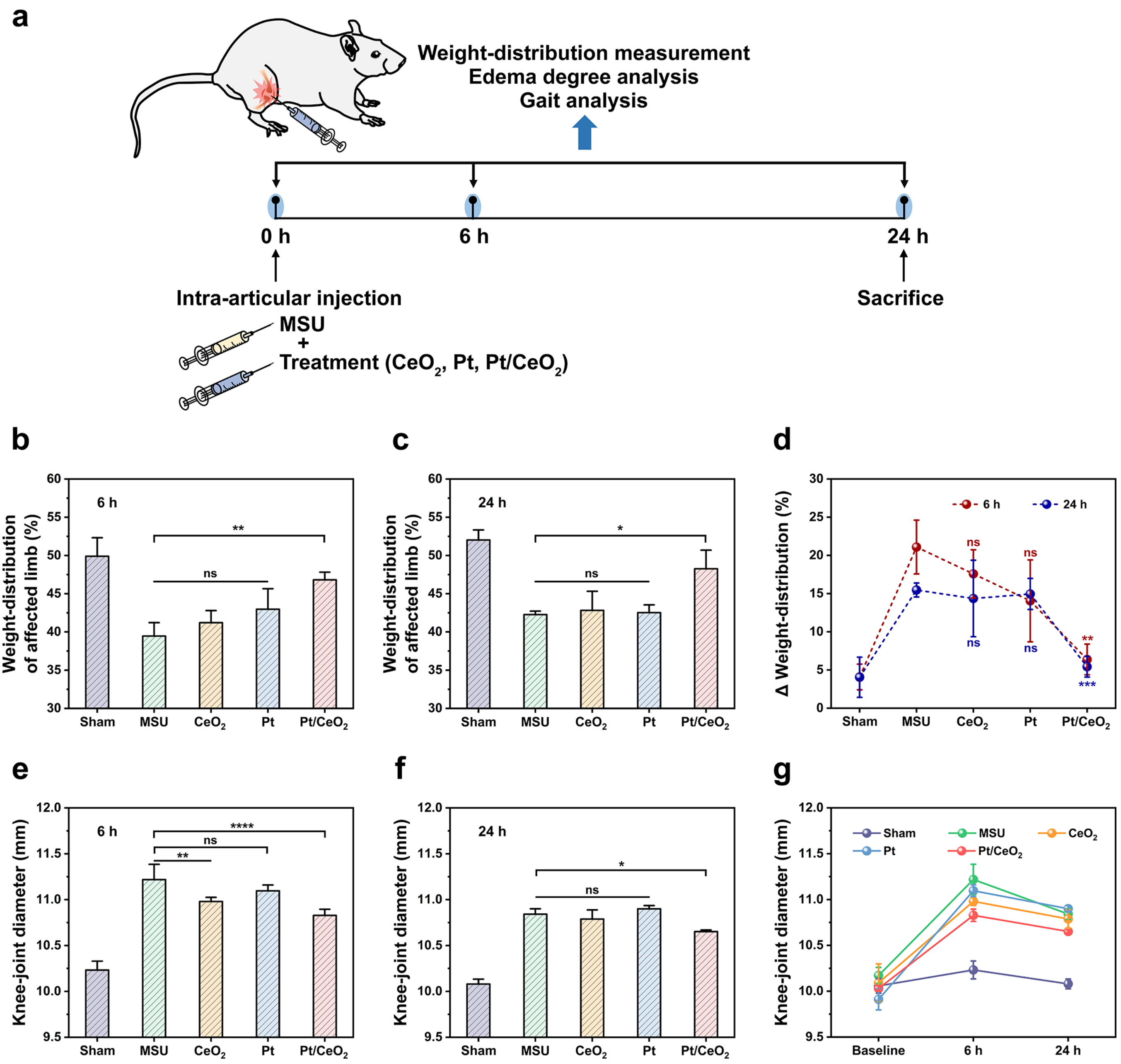

Figure 4. Effects of Pt/CeO_2 on pain response and edema degree in MSU-induced acute gout rats. (a) Experimental scheme of MSU-induced acute gout rats. (b, c) Weight distribution of affected limbs (right hind limbs) of rats at 6 and 24 h, respectively. (d) Differences in weight distribution between bilateral hind limbs of rats at 6 and 24 h. (e, f) Knee-joint diameter of affected limbs of rats at 6 and 24 h, respectively. (g) Variations in knee-joint diameter of the affected limbs of rats. Data are presented as mean ± SD ($n = 5$). Statistical differences were analyzed by one-way ANOVA and Student's t test: $^{*}p < 0.05$, $^{**}p < 0.01$, $^{***}p < 0.001$, $^{****}p < 0.0001$, and ns (not significant).

cascade reaction catalyzed by Pt/CeO_2 is depicted in Figure 3e. Since the detailed mechanism of UA degradation catalyzed by Pt has not been clearly established, different methods of characterization may detect various compounds with different molecular weights.[22]

Then, we investigated the diverse catalytic activities of Pt/CeO_2 with different $n[\mathrm{Pt}]/n[\mathrm{CeO_2}]$ molar ratios to identify the best Pt/CeO_2 ratio (Figure 3f–i and Figures S14 and S15). CeO_2 nanorods and Pt alone without modifications were used as control groups. By monitoring the characteristic absorbance of UA at 292 nm, we observed that both Pt/CeO_2 and Pt alone could efficiently degrade UA during 90 min *in vitro*. As shown in Figure 3f, a higher content of Pt in Pt/CeO_2 was beneficial to the degradation of UA under physiological conditions, though it was slightly inferior to an equal amount of Pt alone. This indicated that Pt played a dominant role in degrading UA.

The ROS scavenging activities of Pt/CeO_2 toward $^{\bullet}O_2^-$ and H_2O_2, the two representative ROS involved in the inflammation of gout, were investigated as shown in Figure 3g,h. We studied the superoxide dismutase (SOD)-like activity for $^{\bullet}O_2^-$ elimination at first. It was obvious that Pt/CeO_2 showed a good combination of Pt and CeO_2 on eliminating $^{\bullet}O_2^-$, whereas an excessive content of Pt in Pt/CeO_2 did not further enhance the SOD-like activity (Figure 3g). Moreover, Pt/CeO_2 (1/5) and Pt/CeO_2 (1/10) had better SOD-like activity in comparison to their equal amounts of Pt alone, respectively.

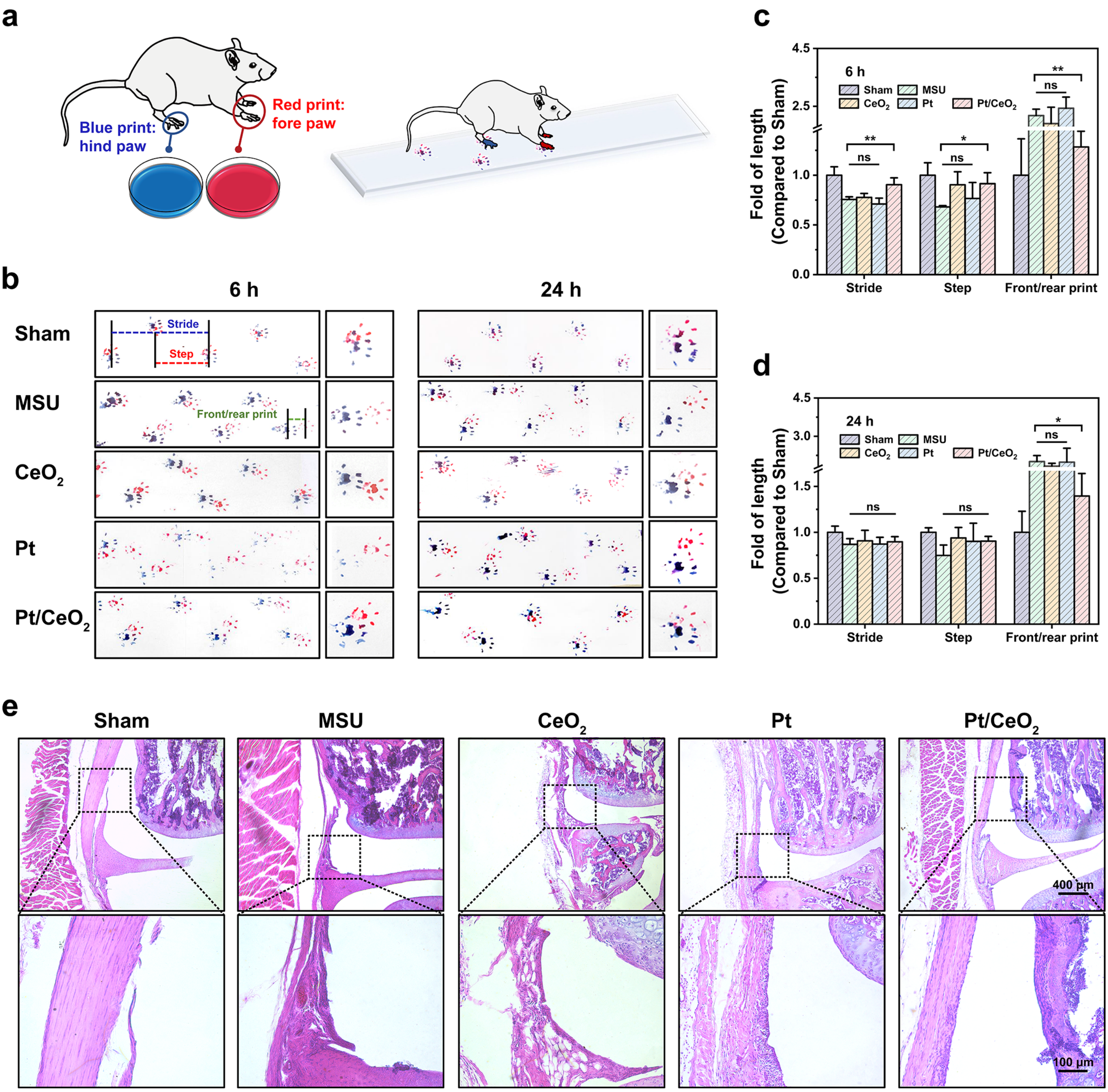

Figure 5. Effects of Pt/CeO$_2$ on gait analysis and H&E staining images of the synovial area in MSU-induced acute gout rats. (a) Experimental design of gait analysis in MSU-induced acute gout rats. Rats with red-inked fore paws and blue-inked hind paws had to run over a 100 cm length, 10 cm width runway, covered with paper. (b) Gait analysis results for different groups. The blue dotted line represents stride length, the red dotted line represents step length, and the green dotted line represents the length of front/rear paw prints: red print, fore paw; blue print, hind paw. (c, d) Quantification of stride length, step length, and the length of front/rear paw prints at 6 and 24 h. Data are presented as mean ± SD ($n = 5$). Statistical differences were analyzed by one-way ANOVA and Student's t test: $^*p < 0.05$, $^{**}p < 0.01$, and ns (not significant). (e) H&E staining images of the synovial area in different groups of MSU-induced acute gout rats. Scale bar: 400 μm in the first row and 100 μm in the second row, respectively.

Then, the CAT-like activity of Pt/CeO$_2$ was also investigated, as shown in Figure 3h. We observed that, as the content of Pt in Pt/CeO$_2$ increased, the capability of degrading H_2O_2 gradually increased until its plateau. In the composite structure, Pt largely contributed to the CAT-like activity while CeO$_2$ showed a negligible effect on degrading H_2O_2 due to the unique rod shape.

The RNS eliminating activity of Pt/CeO$_2$ was investigated using 1,1-diphenyl-2-picrylhydrazyl (DPPH) as a model molecule (Figure S15). We found that Pt in Pt/CeO$_2$ played a dominant role in scavenging DPPH free radicals while CeO$_2$ had a weak capacity. According to the results above, it was suggested that Pt/CeO$_2$ (1/5) showed the best performance of diverse enzyme-like activities and potential possibility for the efficient therapy of gout (Figure 3i). In addition, Pt/CeO$_2$ (1/5) showed good recyclability and stability of diverse activities (Figures S16 and S17).

2.4. Pt/CeO_2 Alleviates Pain and Joint Edema in MSU-Induced Acute Gout Rats. In this study, the detection of cell viability of RAW264.7 and SW982 cell lines induced by Pt, CeO_2, and Pt/CeO_2 with different molar ratios, respectively, was carried out at first (Figures S18 and S19). On the basis of the results of cell viability and catalytic activities, Pt/CeO_2 (1/5) with a Pt concentration of 10 μg/mL was considered to be optimal for cell proliferation in the joint tissues and was used in subsequent animal experiments.

Then, we prepared MSU crystals and characterized them by scanning electron microscope (SEM) images (Figure S20). Afterward, the synthesized MSU was intra-articularly injected into the right knee joint of SD rats to construct an acute gout model. Then saline, Pt, CeO_2, and Pt/CeO_2 solution were intra-articularly injected into the joint in each group separately. Weight-distribution measurements, edema degree analyses, and gait analyses were performed at 6 and 24 h to monitor the pain level of the affected limb (Figure 4a). As shown in Figure 4b,c, the weight distribution of the normal limb was nearly 50% at 6 and 24 h, which represented a baseline. After the injection of MSU, the ratio was significantly decreased at 6 and 24 h, illustrating the weakening in weight bearing of the affected limb caused by pain. After injection of Pt/CeO_2, rather than Pt and CeO_2, the weight distribution on the affected limb was higher at 6 and 24 h in comparison to other groups. These results indicated that Pt/CeO_2 alleviated pain and rebalanced the weight distribution between the two limbs in the process of acute gout. The therapeutic effect was evident 6 h after injection of Pt/CeO_2 (Figure 4d). In addition, we measured the maximum distance between the medial and lateral condyles of the affected limbs to assess the joint edema after the injection. The results showed that Pt/CeO_2 helped relieve joint swelling during the process of acute gout (Figure 4e−g).

2.5. Amelioration of Gait Claudication and Tissue Inflammation with Pt/CeO_2. Rats with red-inked fore paws and blue-inked hind paws were allowed to freely walk from one side to another side on a 100 cm × 10 cm track (Figure 5a). The footprints of the rats' feet were recorded, and a gait analysis during walking clearly revealed the pain of the affected limb. The prints of the front and hind paws of rats in the sham group were relatively overlapping, while those of rats in the MSU group were distinctly separated. The injection of Pt/CeO_2 reduced this tendency and partially restored the movement at 6 and 24 h (Figure 5b). The average stride length and step length of the Pt/CeO_2 group were more similar to those of sham group than to those of other groups at 6 h (Figure 5c), but the results at 24 h were not significant (Figure 5d). In general, an analysis of the gait further elaborated that Pt/CeO_2 relieved pain induced by MSU deposition. In gouty arthritis, cell infiltration is usually accompanied by disease progression and tissue remodeling. An H&E analysis of the synovial tissue was carried out to evaluate the inflammatory cellular recruitment after the MSU injection. As shown in Figure 5e, intra-articular injection of Pt/CeO_2 attenuated the inflammatory cell infiltration into the synovium induced by MSU. When they were taken together, these results indicated that Pt/CeO_2 had a certain therapeutic effect on acute gout, which should provide new insights for gout treatment.

3. CONCLUSION

In summary, the self-cascade nanozyme Pt/CeO_2 with both uricase- and CAT-like activities was developed to tackle the accumulation of MSU and H_2O_2 in joints for gout treatment. The designed Pt/CeO_2 structure ensured the *in situ* growth of Pt with smaller sizes on CeO_2 nanorods, facilitating the long-term retainment of catalytic activity. Importantly, Pt/CeO_2 could not only efficiently degrade UA but also remove the byproduct H_2O_2 in a timely fashion in one catalytic system. Moreover, Pt/CeO_2 (1/5) had excellent capabilities, including UA degradation and ROS and RNS scavenging activities. In the MSU-induced acute gout model, Pt/CeO_2 nanozyme alleviated pain along with joint edema *in vivo*, thus improving gait claudication and tissue inflammation. This work presents the potential of a nanozyme as a therapeutic agent for the effective treatment of gout, providing a new strategy to develop enzyme-like therapy.

■ ASSOCIATED CONTENT

Supporting Information

The Supporting Information is available free of charge at https://pubs.acs.org/doi/10.1021/acs.nanolett.1c04454.

Materials, methods, and additional figures and tables as described in the text (PDF)

■ AUTHOR INFORMATION

Corresponding Authors

Dongquan Shi − *State Key Laboratory of Pharmaceutical Biotechnology, Department of Sports Medicine and Adult Reconstructive Surgery, Nanjing Drum Tower Hospital, The Affiliated Hospital of Nanjing University Medical School, Nanjing, Jiangsu 210008, People's Republic of China;* orcid.org/0000-0002-4769-7816; Email: shidongquan@nju.edu.cn

Hui Wei − *Department of Biomedical Engineering, College of Engineering and Applied Sciences, Nanjing National Laboratory of Microstructures, Jiangsu Key Laboratory of Artificial Functional Materials, Nanjing University, Nanjing, Jiangsu 210023, People's Republic of China; State Key Laboratory of Analytical Chemistry for Life Science, School of Chemistry and Chemical Engineering, Chemistry and Biomedicine Innovation Center (ChemBIC), Nanjing University, Nanjing, Jiangsu 210023, People's Republic of China;* orcid.org/0000-0003-0870-7142; Email: weihui@nju.edu.cn

Authors

Anqi Lin − *State Key Laboratory of Pharmaceutical Biotechnology, Department of Sports Medicine and Adult Reconstructive Surgery, Nanjing Drum Tower Hospital, The Affiliated Hospital of Nanjing University Medical School, Nanjing, Jiangsu 210008, People's Republic of China; Department of Biomedical Engineering, College of Engineering and Applied Sciences, Nanjing National Laboratory of Microstructures, Jiangsu Key Laboratory of Artificial Functional Materials, Nanjing University, Nanjing, Jiangsu 210023, People's Republic of China*

Ziying Sun − *State Key Laboratory of Pharmaceutical Biotechnology, Department of Sports Medicine and Adult Reconstructive Surgery, Nanjing Drum Tower Hospital, The Affiliated Hospital of Nanjing University Medical School, Nanjing, Jiangsu 210008, People's Republic of China*

Xingquan Xu − *State Key Laboratory of Pharmaceutical Biotechnology, Department of Sports Medicine and Adult Reconstructive Surgery, Nanjing Drum Tower Hospital, The*

Affiliated Hospital of Nanjing University Medical School, Nanjing, Jiangsu 210008, People's Republic of China

Sheng Zhao – *Department of Biomedical Engineering, College of Engineering and Applied Sciences, Nanjing National Laboratory of Microstructures, Jiangsu Key Laboratory of Artificial Functional Materials, Nanjing University, Nanjing, Jiangsu 210023, People's Republic of China*

Jiawei Li – *State Key Laboratory of Pharmaceutical Biotechnology, Department of Sports Medicine and Adult Reconstructive Surgery, Nanjing Drum Tower Hospital, The Affiliated Hospital of Nanjing University Medical School, Nanjing, Jiangsu 210008, People's Republic of China*

Heng Sun – *State Key Laboratory of Pharmaceutical Biotechnology, Department of Sports Medicine and Adult Reconstructive Surgery, Nanjing Drum Tower Hospital, The Affiliated Hospital of Nanjing University Medical School, Nanjing, Jiangsu 210008, People's Republic of China*

Quan Wang – *Department of Biomedical Engineering, College of Engineering and Applied Sciences, Nanjing National Laboratory of Microstructures, Jiangsu Key Laboratory of Artificial Functional Materials, Nanjing University, Nanjing, Jiangsu 210023, People's Republic of China*

Qing Jiang – *State Key Laboratory of Pharmaceutical Biotechnology, Department of Sports Medicine and Adult Reconstructive Surgery, Nanjing Drum Tower Hospital, The Affiliated Hospital of Nanjing University Medical School, Nanjing, Jiangsu 210008, People's Republic of China;* orcid.org/0000-0002-2552-9686

Complete contact information is available at:
https://pubs.acs.org/10.1021/acs.nanolett.1c04454

Author Contributions

A.L., Z.S., X.X., S.Z., and Q.J. designed the study. H.W. and D.S. guided the study. A.L. designed and synthesized the materials, performed the *in vitro* study, and analyzed the data. Z.S. performed the cellular experiments and analyzed the data. Z.S. and X.X. designed the *in vivo* animal model. Z.S. and A.L. performed the *in vivo* study. S.Z. and Q.W. assisted with the *in vitro* study and data analysis. J.L., H.S., and Q.J. assisted with the *in vivo* study. The manuscript was written through contributions of all authors. All authors have given approval to the final version of the manuscript.

Author Contributions

[‖]A.L. and Z.S. contributed equally to this work.

Funding

This work was supported by National Key R&D Program of China (2018YFC1105904 and 2019YFA0709200), the Key Program of the NSFC (81730067), the National Natural Science Foundation of China (81772335 and 21874067), the Natural Science Foundation of Jiangsu Province (BK20180127), the PAPD Program, and Fundamental Research Funds for the Central Universities (021314380195).

Notes

The authors declare no competing financial interest.

ACKNOWLEDGMENTS

The authors thank Quanyi Liu for valuable advice in the schematic illustration.

REFERENCES

(1) Roddy, E.; Doherty, M. Epidemiology of gout. *Arthritis Res. Ther.* **2010**, *12*, 223.

(2) Rees, F.; Hui, M.; Doherty, M. Optimizing current treatment of gout. *Nat. Rev. Rheumatol.* **2014**, *10*, 271–283.

(3) Dehlin, M.; Jacobsson, L.; Roddy, E. Global epidemiology of gout: prevalence, incidence, treatment patterns and risk factors. *Nat. Rev. Rheumatol.* **2020**, *16*, 380–390.

(4) Terkeltaub, R. A. Gout. *N. Engl. J. Med.* **2003**, *349*, 1647–1655.

(5) Rock, K. L.; Kataoka, H.; Lai, J. J. Uric acid as a danger signal in gout and its comorbidities. *Nat. Rev. Rheumatol.* **2013**, *9*, 13–23.

(6) Kuo, C. F.; Grainge, M. J.; Zhang, W.; Doherty, M. Global epidemiology of gout: prevalence, incidence and risk factors. *Nat. Rev. Rheumatol.* **2015**, *11*, 649–662.

(7) Dalbeth, N.; Merriman, T. R.; Stamp, L. K. Gout. *Lancet* **2016**, *388*, 2039–2052.

(8) Sherman, M. R.; Saifer, M. G.; Perez-Ruiz, F. PEG-uricase in the management of treatment-resistant gout and hyperuricemia. *Adv. Drug Delivery Rev.* **2008**, *60*, 59–68.

(9) Tan, Q.; Zhang, J.; Wang, N.; Li, X.; Xiong, H.; Teng, Y.; He, D.; Wu, J.; Zhao, C.; Yin, H.; et al. Uricase from Bacillus fastidious loaded in alkaline enzymosomes: enhanced biochemical and pharmacological characteristics in hypouricemic rats. *Eur. J. Pharm. Biopharm.* **2012**, *82*, 43–48.

(10) Xiong, H.; Zhou, Y.; Zhou, Q.; He, D.; Wan, S.; Tan, Q.; Zhang, M.; Deng, X.; Zhang, J. Nanosomal microassemblies for highly efficient and safe delivery of therapeutic enzymes. *ACS Appl. Mater. Interfaces* **2015**, *7*, 20255–20263.

(11) Zhang, P.; Jain, P.; Tsao, C.; Yuan, Z.; Li, W.; Li, B.; Wu, K.; Hung, H. C.; Lin, X.; Jiang, S. Polypeptides with high zwitterion density for safe and effective therapeutics. *Angew. Chem., Int. Ed.* **2018**, *57*, 7743–7747.

(12) Terkeltaub, R. Update on gout: new therapeutic strategies and options. *Nat. Rev. Rheumatol.* **2010**, *6*, 30–38.

(13) Nuki, G. Uricase therapy of gout. In *Gout & Other Crystal Arthropathies*; Elsevier: **2012**; pp 174–186.

(14) Liu, X.; Zhang, Z.; Zhang, Y.; Guan, Y.; Liu, Z.; Ren, J.; Qu, X. Artificial metalloenzyme-based enzyme replacement therapy for the treatment of hyperuricemia. *Adv. Funct. Mater.* **2016**, *26*, 7921–7928.

(15) Zhang, Z.; Gu, Y.; Liu, Q.; Zheng, C.; Xu, L.; An, Y.; Jin, X.; Liu, Y.; Shi, L. Spatial confined synergistic enzymes with enhanced uricolytic performance and reduced toxicity for effective gout treatment. *Small* **2018**, *14*, No. 1801865.

(16) Kim, S.; Kim, M.; Jung, S.; Kwon, K.; Park, J.; Kim, S.; Kwon, I.; Tae, G. Co-delivery of therapeutic protein and catalase-mimic nanoparticle using a biocompatible nanocarrier for enhanced therapeutic effect. *J. Controlled Release* **2019**, *309*, 181–189.

(17) Zhang, L.; Zhang, C.; Zhuang, Z.; Li, C.; Pan, P.; Zhang, C.; Zhang, X. Bio-inspired nanoenzyme for metabolic reprogramming and anti-inflammatory treatment of hyperuricemia and gout. *Sci. China Chem.* **2021**, *64*, 616–628.

(18) Huang, L.; Chen, J.; Gan, L.; Wang, J.; Dong, S. Single-atom nanozymes. *Sci. Adv.* **2019**, *5*, No. eaav5490.

(19) Tonga, G. Y.; Jeong, Y.; Duncan, B.; Mizuhara, T.; Mout, R.; Das, R.; Kim, S. T.; Yeh, Y. C.; Yan, B.; Hou, S.; et al. Supramolecular regulation of bioorthogonal catalysis in cells using nanoparticle-embedded transition metal catalysts. *Nat. Chem.* **2015**, *7*, 597–603.

(20) Zhang, Z.; Zhang, X. D.; Liu, B.; Liu, J. Molecular imprinting on inorganic nanozymes for hundred-fold enzyme specificity. *J. Am. Chem. Soc.* **2017**, *139*, 5412–5419.

(21) Xi, J.; Zhang, R.; Wang, L.; Xu, W.; Liang, Q.; Li, J.; Jiang, J.; Yang, Y.; Yan, X.; Fan, K.; et al. A nanozyme-based artificial peroxisome ameliorates hyperuricemia and ischemic stroke. *Adv. Funct. Mater.* **2021**, *31*, 2007130.

(22) Dong, Y.; Chi, Y.; Lin, X.; Zheng, L.; Chen, L.; Chen, G. Nano-sized platinum as a mimic of uricase catalyzing the oxidative degradation of uric acid. *Phys. Chem. Chem. Phys.* **2011**, *13*, 6319–6324.

(23) Devi, H. S.; Singh, H. P. Unique dual responsive activity of a platinum nanozyme stabilized by a green solvent: deep eutectic solvents. *New J. Chem.* **2018**, *42*, 12369–12373.

(24) Fan, J.; Yin, J. J.; Ning, B.; Wu, X.; Hu, Y.; Ferrari, M.; Anderson, G. J.; Wei, J.; Zhao, Y.; Nie, G. Direct evidence for catalase and peroxidase activities of ferritin-platinum nanoparticles. *Biomaterials* **2011**, *32*, 1611−1618.

(25) Su, H.; Liu, D. D.; Zhao, M.; Hu, W. L.; Xue, S. S.; Cao, Q.; Le, X. Y.; Ji, L. N.; Mao, Z. W. Dual-enzyme characteristics of polyvinylpyrrolidone-capped iridium nanoparticles and their cellular protective effect against H_2O_2-induced oxidative damage. *ACS Appl. Mater. Interfaces* **2015**, *7*, 8233−8242.

(26) Baran, T.; Inanan, T.; Mentes, A. Synthesis, characterization, and catalytic activity in Suzuki coupling and catalase-like reactions of new chitosan supported Pd catalyst. *Carbohyd. Polym.* **2016**, *145*, 20−29.

(27) Miao, Z.; Jiang, S.; Ding, M.; Sun, S.; Ma, Y.; Younis, M. R.; He, G.; Wang, J.; Lin, J.; Cao, Z.; et al. Ultrasmall rhodium nanozyme with RONS scavenging and photothermal activities for anti-inflammation and antitumor theranostics of colon diseases. *Nano Lett.* **2020**, *20*, 3079−3089.

(28) Nie, L.; Mei, D.; Xiong, H.; Peng, B.; Ren, Z.; Hernandez, X. I. P.; DeLaRiva, A.; Wang, M.; Engelhard, M. H.; Kovarik, L.; et al. Activation of surface lattice oxygen in single-atom Pt/CeO_2 for low-temperature CO oxidation. *Science* **2017**, *358*, 1419−1423.

(29) Yan, R.; Sun, S.; Yang, J.; Long, W.; Wang, J.; Mu, X.; Li, Q.; Hao, W.; Zhang, S.; Liu, H.; et al. Nanozyme-based bandage with single-atom catalysis for brain trauma. *ACS Nano* **2019**, *13*, 11552−11560.

(30) Jiang, F.; Wang, S.; Liu, B.; Liu, J.; Wang, L.; Xiao, Y.; Xu, Y.; Liu, X. Insights into the influence of CeO_2 crystal facet on CO_2 hydrogenation to methanol over Pd/CeO_2 catalysts. *ACS Catal.* **2020**, *10*, 11493−11509.

(31) Zhao, S.; Kang, D.; Liu, Y.; Wen, Y.; Xie, X.; Yi, H.; Tang, X. Spontaneous formation of asymmetric oxygen vacancies in transition-metal-doped CeO_2 nanorods with improved activity for carbonyl sulfide hydrolysis. *ACS Catal.* **2020**, *10*, 11739−11750.

(32) Wu, J.; Wang, X.; Wang, Q.; Lou, Z.; Li, S.; Zhu, Y.; Qin, L.; Wei, H. Nanomaterials with enzyme-like characteristics (nanozymes): next-generation artificial enzymes (II). *Chem. Soc. Rev.* **2019**, *48*, 1004−1076.

(33) Yu, T.; Lim, B.; Xia, Y. Aqueous-phase synthesis of single-crystal ceria nanosheets. *Angew. Chem., Int. Ed.* **2010**, *49*, 4484−4487.

(34) Li, J.; Zhang, Z.; Tian, Z.; Zhou, X.; Zheng, Z.; Ma, Y.; Qu, Y. Low pressure induced porous nanorods of ceria with high reducibility and large oxygen storage capacity: synthesis and catalytic applications. *J. Mater. Chem. A* **2014**, *2*, 16459−16466.

(35) Yang, Z.; Luo, S.; Zeng, Y.; Shi, C.; Li, R. Albumin-mediated biomineralization of shape-controllable and biocompatible ceria nanomaterials. *ACS Appl. Mater. Interfaces* **2017**, *9*, 6839−6848.

(36) Zhang, Z.; Wang, Z.; Li, Z.; Zheng, W.; Fan, L.; Zhang, J.; Hu, Y.; Luo, M.; Wu, X.; Gong, X.; et al. Metal-free ceria catalysis for selective hydrogenation of crotonaldehyde. *ACS Catal.* **2020**, *10*, 14560−14566.

(37) Meng, F.; Wang, L.; Cui, J. Controllable synthesis and optical properties of nano-CeO_2 via a facile hydrothermal route. *J. Alloys Compd.* **2013**, *556*, 102−108.

(38) Guo, W.; Zhang, M.; Lou, Z.; Zhou, M.; Wang, P.; Wei, H. Engineering nanoceria for enhanced peroxidase mimics: a solid solution strategy. *ChemCatChem.* **2019**, *11*, 737−743.

(39) Svintsitskiy, D. A.; Kibis, L. S.; Stadnichenko, A. I.; Koscheev, S. V.; Zaikovskii, V. I.; Boronin, A. I. Highly oxidized platinum nanoparticles prepared through radio-frequency sputtering: thermal stability and reaction probability towards CO. *ChemPhysChem* **2015**, *16*, 3318−3324.

(40) Stadnichenko, A. I.; Muravev, V. V.; Koscheev, S. V.; Zaikovskii, V. I.; Aleksandrov, H. A.; Neyman, K. M.; Boronin, A. I. Study of active surface centers of Pt/CeO_2 catalysts prepared using radio-frequency plasma sputtering technique. *Surf. Sci.* **2019**, *679*, 273−283.

(41) Maheswari, A. U.; Anjali, K. K.; Sivakumar, M. Optical absorption enhancement of PVP capped TiO_2 nanostructures in the visible region. *Solid State Ion.* **2019**, *337*, 33−41.

(42) Wang, X.; Kang, Q.; Li, D. Low-temperature catalytic combustion of chlorobenzene over MnO_x-CeO_2 mixed oxide catalysts. *Catal. Commun.* **2008**, *9*, 2158−2162.